Tech Science Press

# Simulation Analysis on Mechanical Property Characterization of Carbon Nanotubes Reinforced Epoxy Composites

**Dan Li[1], Li Ding[1], Zhengang Liu[2], Qiang Li[3], Kaiyun Guo[1] and Hailin Cao[1,4,*]**

[1]Shenzhen Academy of Aerospace Technology, Shenzhen, 518057, China
[2]Shanghai Aerospace Control Technology Institute, Shanghai, 201109, China
[3]Shanghai Institute of Satellite Engineering, Shanghai, 201109, China
[4]Harbin Institute of Technology (Shenzhen), Shenzhen, 518055, China
[*]Corresponding Author: Hailin Cao. Email: caohl@hit.edu.cn

**Abstract:** Carbon nanotube (CNT)-reinforced composites have ultra-high elastic moduli, low densities, and fibrous structures. This paper presents the multi-scale finite element modeling of CNT-reinforced polymer composites from micro- to macro-scales. The nanocomposites were modeled using representative volume elements (RVEs), and finite element code was written to simulate the modeling and loading procedure and obtain equivalent mechanical properties of the RVEs with various volume fractions of CNTs, which can be used directly in the follow-up simulation studies on the macroscopic model of CNT-reinforced nanocomposites. When using the programming to simulate the deformation and fracture process of the CNT-reinforced epoxy composites, the mechanical parameters and stress-strain curves of the composites on the macro-scale were obtained by endowing the elements of the lattice models with RVE parameters. Tensile experiments of the CNT-reinforced composites were also carried out. The validity of the finite element simulation method was verified by comparing the results of the simulations and experiments. Finite element models of functionally graded CNT-reinforced composites (FG-CNTRC) with different distributions were established, and the tensile and three-point-bending conditions for various graded material models were simulated by the methods of lattice model and birth-death element to obtain the tensile and bending parameters. In addition, the influence of the distribution and volume ratio of the CNTs on the performance of the graded composite material structures was also analyzed.

**Keywords:** Finite element method; lattice modeling; carbon nanotube; mechanical properties; gradient composites

## 1 Introduction

Carbon nanotubes (CNTs) are coaxial tubular structures formed by the intertangling of hexagonal grids that are made up of carbon atoms [1]. Their radial dimensions are at the nanometer level, and their lengths can reach the micron level. Such unique structures lead to unique mechanical, thermal and electromagnetic properties of CNTs [2–7], which make them ideal

one-dimensional functional materials. The tensile strengths of CNTs can reach 102 GPa, and their moduli can reach the magnitude of TPa [8,9]. At the same time, the CNT density is extremely low. Based on their excellent mechanical performance, CNTs can be used as a reinforcing phase to enhance the mechanical properties of polymers, metals, and ceramics [10–17]. Moreover, another superiority of CNTs as reinforcement materials is their large surface-area-to-volume ratios, which improve the adhesion with the polymeric matrix, thereby enhancing the composite properties [18]. CNTs have far better enhancement abilities compared to those of traditional carbon fibers, and using CNTs as a reinforcing phase can yield lighter and stronger composites. In general, the basic mechanical parameters of the CNTs are obtained by experimental means. However, when it comes to broader material performance studies, such as studies of the thermal and vibration behaviors, there are many limitations on the testing equipment and techniques because of the very small scales of CNTs. The molecular dynamics (MD) method is regarded as one of the most effective and reliable methods in the study of nanoscale materials [19–24]. Numerous investigations on the mechanical behaviors and physiochemical properties of CNTs, such as the tensile characteristics [19], buckling [20,21], thermal properties [22], and vibration behaviors [23,24], have been conducted using MD simulation approaches. These studies provided important parameters for designing and analyzing more efficient nanocomposites.

Many experimental and simulation methods have been utilized to investigate the mechanical properties of the CNT-reinforced polymer composites [25]. The experimental methods include indentation tests [26] and rheological tests [25]. In general, the simulation methods are either MD simulations [15–17] or finite element analysis (FEA) based on continuum mechanics models at different scales [25,27–33]. Sharma et al. [15] examined the mechanical properties of multi-walled CNT-polycarbonate composites by employing the MD technique. Chawla et al. [16] surveyed the effect of CNT pull-out from the polyethylene (PE) matrix on the mechanical properties of CNT/PE composites. Hu et al. [18] proposed using representative volume elements (RVEs) and 3-D microscale unit cells to effectively predict the mechanical properties of CNT-modified polymeric nanocomposites. A multiscale finite element modeling approach was devised by Gupta et al. [34] to investigate the pinhole defects inside CNT-reinforced polymer composites. Grabowski et al. [35] rendered a new multiscale electro-mechanical framework for the numerical modeling of composite materials reinforced by CNTs that are used in strain sensors. Palacios et al. [36,37] studied the dynamic response of a carbon-nanotube-reinforced-polymer (CNRP) material and determined the reliability and hazards based on its mechanical properties by developing a 3D multiscale finite element model of the RVEs of the nanocomposite.

Functionally graded materials (FGMs) are heterogeneous composites, and the volume content of the enhancer is spatially arranged in the gradient, which gives this material good designability and maximizes the enhancement effect of the reinforcement [38,39]. Functionally graded CNT-reinforced composites (FG-CNTRCs) are a new type of FGM in which CNTs are functionally graded in the thickness direction [40] to improve the mechanical or thermal properties of the composites further. Their material behaviors have become popular research subjects in recent years [41–46]. Shen [47] first proposed CNT-based FGMs with CNT-graded distributions to improve the properties of structures. Kwon et al. [48] prepared real functionally gradient CNT-reinforced composites in the laboratory. Jiao et al. [41] investigated the buckling behaviors of thin FG-CNTR plates with rectangular shapes to bear compression loads arbitrarily distributed on the partial edges.

However, at the present stage, it is still difficult to form an effective support for the accurate characterization of a material's macroscopic properties by integrating the research results related

to the mechanical properties of CNT-reinforced composites, which creates an obstacle for guiding the material and structural design effectively. For CNT-reinforced polymer matrix composites, the heterogeneity of their structures was demonstrated by electron microscopy images and experimental results, such as the distribution direction of the CNTs and the material density. The randomness, which was caused by the heterogeneity of the composite structures, also affected the overall and local performances of the composites. In the present work, the multi-scale models of carbon nanotubes, interfaces, and matrix materials were established to carry out the analysis of the mechanical properties of CNT-reinforced epoxy composites. A finite element model of FG-CNTRCs with different distributions was established, and the tensile and three-point-bending experiments for various graded material models were simulated to obtain the parameters, such as the bending modulus. In addition, the influences of the distributions and volume ratios of the CNTs on the performances of the FG-CNTRCs were also analyzed.

## 2 Mechanical Properties for RVEs

### 2.1 Modeling of RVEs

Many studies have shown that the CNT length has a significant effect on the effective mechanical properties of fiber-enhanced composites. Although the length has little influence on the effective shear modulus, it has a significant impact on the equivalent elastic modulus. As the CNT length increases, the force transfer efficiency of the composite material is also enhanced significantly. In general studies of fiber-reinforced composites, based on the different lengths of the fibers, two types of models are generally established, in which the fiber length is equal to or less than the matrix dimension. In addition, the nanoscale RVEs can also be divided into three types based on their cross sections, which are circular, square, and hexagonal shapes. Thus, six forms of RVEs were used in this study. The averaged data of the RVEs with three cross sections represent the equivalent mechanical properties of the nanocomposites with nano-heterostructures. Each RVE comprises three components: a CNT, interface, and matrix composed of polymer resin. The schematic diagram of an RVE with a circular section is shown in Fig. 1, in which a1 is the inner diameter of the CNT, a2 is the outer diameter of the CNT, a3 is the external diameter of the interface layer, and a4 is the outer dimension of the matrix.
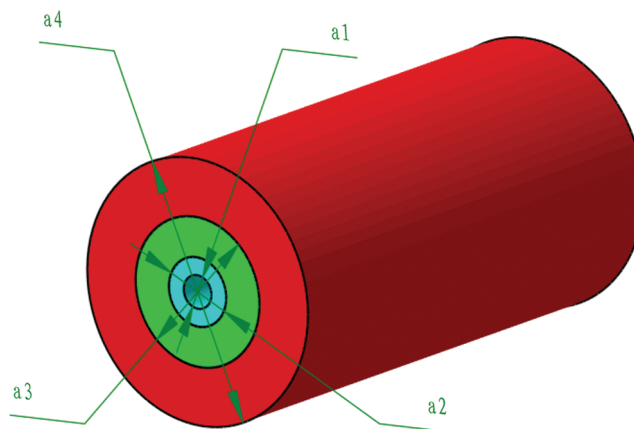


**Figure 1:** Schematic diagram of an RVE with a circular section

Most CNTs have diameters of 1.2–1.4 nm, and the thickness of the interface layer can range from 0.2–3 nm [18]. However, in most situations, the interphase thickness changes from 0.5 to 4 times the thickness of the CNT. In this study, the interphase thickness was set to 2.25 times the CNT thickness, which was the intermediate value. Mechanical properties of the interface were obtained using the relevant equations. The average value of the elastic modulus of the interphase can be calculated by [18]

$$E^{\text{int}} = \frac{2}{r_{\text{int}} + r_0} \left[ E^{\text{m}} r_{\text{int}} + \left( E^{\text{t}} - E^{\text{m}} \frac{r_{\text{int}}}{r_0} \right) \left( \frac{r_{\text{int}}}{n+1} - \frac{r_{\text{int}} - r_0}{n+2} \right) \right] \tag{1}$$

where $r_{\text{int}}$ and $r_0$ are the inner radii of the interphase and CNT, $E^{\text{m}}$ and $E^{\text{t}}$ are Young's moduli of the matrix and CNT, and $n$ is the interphase enhancement index, which is taken by 50 according to the reference [18]. CNTs with a density of 1.8 g/cm$^3$ and epoxy resin with a density of 1.2 g/cm$^3$ were used in the simulations. The solid geometry model of the RVE was disassembled by ten-node tetrahedron elements whose input data included isotropic material parameters. The required parameters of the finite element model are presented in Tab. 1. The proper element size and total number of elements were selected to ensure that the simulation results were mesh-independent.

**Table 1:** Material and geometric parameters of each component [18]

|           | $E$ (GPa) | $\nu$ | Inner radius (nm) | Thickness (nm) |
|-----------|-----------|-------|-------------------|----------------|
| CNT       | 1054      | 0.40  | 0.315             | 0.335          |
| Interface | 16.10     | 0.40  | 0.65              | 0.754          |
| Matrix    | 2.026     | 0.25  | 1.404             | –              |

Several assumptions were made to study the CNT-reinforced composites. First, for polymer matrix composites where the CNTs were distributed randomly, the stress-strain relationship of the material microstructure units was linear, and the elements were transversely isotropic. Although the CNTs were randomly distributed in the composites overall, the composites were regarded as a homogeneous material at a certain scale. Second, the microstructural units of the composite materials were subjected to unidirectional loading. The forces applied on the model were uniaxial tensile, radial expanding, and torsion forces. Finally, the agglomeration effect and bending of the CNTs in the composites were not considered. Some related studies showed that the bending and agglomeration of CNTs have relatively little performance impact on the composites when the CNT content is low. According to the theory of elasticity, the constitutive equation of the transverse isotropic composite material can be written as

$$\begin{Bmatrix} \varepsilon_{\text{x}} \\ \varepsilon_{\text{y}} \\ \varepsilon_{\text{z}} \end{Bmatrix} = \begin{bmatrix} \dfrac{1}{E_{\text{x}}} & -\dfrac{\nu_{\text{xy}}}{E_{\text{x}}} & -\dfrac{\nu_{\text{zx}}}{E_{\text{z}}} \\ -\dfrac{\nu_{\text{xy}}}{E_{\text{x}}} & \dfrac{1}{E_{\text{x}}} & -\dfrac{\nu_{\text{zx}}}{E_{\text{z}}} \\ -\dfrac{\nu_{\text{zx}}}{E_{\text{z}}} & -\dfrac{\nu_{\text{zx}}}{E_{\text{z}}} & \dfrac{1}{E_{\text{z}}} \end{bmatrix} \begin{Bmatrix} \sigma_{\text{x}} \\ \sigma_{\text{y}} \\ \sigma_{\text{z}} \end{Bmatrix} \tag{2}$$

The equivalent material properties, such as $E_{\text{x}}$, $E_{\text{z}}$, $\nu_{\text{xy}}$ and $\nu_{\text{zx}}$, can be obtained by computing the deformation and stresses of the RVEs under the load cases of uniaxial tension, lateral

expansion and axial torsion [18]. First of all, a uniaxial tension $\Delta L$ is exerted on the RVEs, which leads to a lateral contraction of $\Delta a$ ($\Delta a < 0$), as shown in Fig. 2a. In this uniaxial load case, the stress and strain components on the plane of $z = L/2$ can be expressed as

$$\begin{cases} \sigma_x = \sigma_y = 0 \\ \varepsilon_x = \varepsilon_y = \Delta a/a \\ \varepsilon_z = \Delta L/L \end{cases} \tag{3}$$

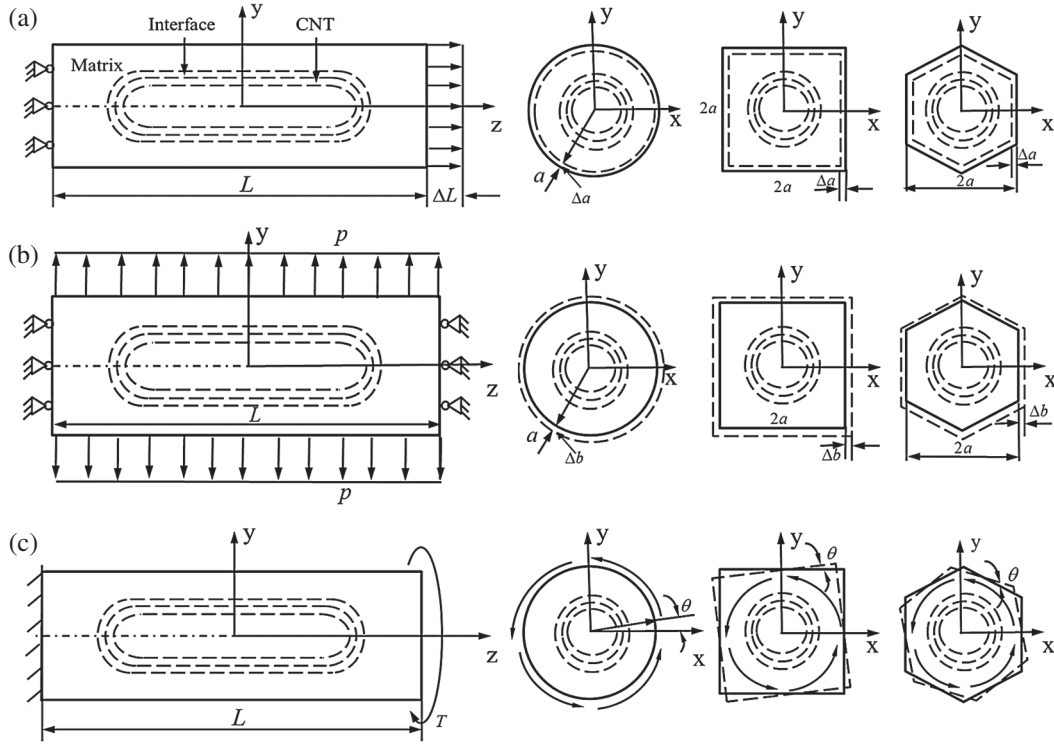The axial elastic modulus $E_z$ can be described as



**Figure 2:** Short CNT RVEs under three loading conditions (a) uniaxial tensile; (b) lateral expansion; and (c) axial torsion

$$E_z = \frac{\sigma_z}{\varepsilon_z} = \frac{L}{\Delta L}\overline{\sigma}_z \tag{4}$$

where $\overline{\sigma}_z$ denotes the axial average stress, which can be obtained by averaging the FEA results. From Eqs. (2) and (3), we get

$$\varepsilon_x = -v_{zx}\frac{\sigma_z}{E_z} = -v_{zx}\frac{\Delta L}{L} = \frac{\Delta a}{a} \tag{5}$$

Hence, the Poisson's ratio $v_{zx}$ is given by

$$v_{zx} = \left(\frac{\Delta a}{a}\right)\bigg/\left(\frac{\Delta L}{L}\right) \tag{6}$$

Then, the RVEs withstands a negative pressure $p$, and both ends of the models in the $z$ direction are constrained, which results in a lateral uniform expansion of $\Delta b$, as shown in Fig. 2b. When the RVEs are under the hydrostatic pressure of $-p$, the stress and strain components can be expressed as

$$\begin{cases} \sigma_x = \sigma_y = p \\ \varepsilon_x = \varepsilon_y = \dfrac{p}{E_x} - \dfrac{v_{xy}p}{E_x} - \dfrac{v_{zx}\sigma_z}{E_z} = \dfrac{\Delta b}{a} \\ \varepsilon_z = -\dfrac{2v_{zx}p}{E_z} + \dfrac{\sigma_z}{E_z} = 0 \end{cases} \tag{7}$$

Thus, there is a relational expression between the elastic modulus ($E_x$ and $E_z$) and Poisson's ratio ($v_{zx}$ and $v_{xy}$) which can be written as

$$\frac{1}{E_x} - \frac{v_{xy}}{E_x} - \frac{2v_{zx}^2}{E_z} = \frac{\Delta b}{pa} \tag{8}$$

Moreover, the Poisson's ratio $v_{xz}$ can be derived from

$$v_{xz} = v_{zx}\frac{E_x}{E_z} \tag{9}$$

Finally, there is a torque $T$ applied on one end of the RVEs, and the other end of the models is fixed, which causes a torsion angle of $\theta$ at the loading end, as shown in Fig. 2c. The shear modulus $G_{xy}$ can be obtained by [18]

$$G_{xy} = \frac{TL}{\theta J} = \frac{E_x}{2(1 + v_{xy})} \tag{10}$$

where $J$ is the average polar moment of inertia of the cross section, whose calculating formulas of the RVEs with circular, square, and hexagonal cross sections are $J = \frac{\pi a^4}{4}$, $J = \frac{8a^4}{3}$ and $J = \frac{10\sqrt{3}a^4}{9}$, respectively. Because the values of $E_z$ and $v_{zx}$ can be calculated by solving Eqs. (4) and (6), the elastic modulus $E_x$ and Poisson's ratio $v_{xy}$ can be determined by Eqs. (8) and (10).

In the present study, finite element code was written to simulate the modeling and loading procedure of the RVEs, and the material parameters were also calculated through this procedure. As long as the CNT volume fraction was input, the modulus and Poisson's ratio of the RVEs could be output after running the finite element software. The models of six kinds of RVEs are shown in Fig. 3.

### 2.2 Results and Discussion

The results of the RVEs with three cross sections were averaged to obtain the equivalent parameters of two kinds of RVEs in which the CNTs were penetrating or embedded types. The simulation results are presented in Tabs. 2 and 3. The results are also compared with pertinent literature results [18] in these tables. The material data obtained above laid a foundation for subsequent research on the macroscopic mechanical properties of CNT-reinforced composites. It can be seen from Tab. 2 that the values of $E_x$, $E_y$, $G_{xy}$ and $v_{xz}$ of the cylindrical RVEs with long CNTs were mostly in the upper bound among the three kinds of RVEs, and these data of the square RVEs were in the lower bound. In addition, the values of $v_{xy}$ of the square RVEs were

basically in the upper bound, and the corresponding data of the cylindrical RVEs were in the opposite boundary. The data of the RVEs with hexagon sections were mostly in the middle range. We can also find that $E_z$ and $\nu_{zx}$ of the three RVEs were almost the same. But in general, the material parameters of these three RVEs are very close and representative. Hence, the averaged data for these three RVEs were used to represent the equivalent mechanical properties of the nanocomposites with long CNTs. From the theory of material mechanics and elastic theory, it can be known that when a torque is applied on one end of a cylinder with uniform circular cross sections, each circular section of the cylinder is maintained as a plane, which only turns an angle around the z axis in the original plane, and the size and shape of the circular sections remain unchanged. However, for the columns with non-circular sections such as the rectangular or hexagon sections, when suffering the twisting forces, the cross sections in the columns rotate around the z axis in their own planes, and warping deformation along the z axis is generated in the cross sections. Because the warping deformation has little influence on the calculation of performance parameters, the torsional deformation of the cross sections around the z axis in the three types of RVEs is only taken into account in the process of simulation and calculation, and corresponding calculation results are in agreement with the results in reference [18], which also proves the feasibility of this treatment. Furthermore, the mechanical parameters of the RVEs are interrelated such as $G_{xy}$, $E_x$ and $\nu_{xz}$, which can be known from the Eqs. (7)–(10). Thus, the different torsional deformations of three kinds of RVEs may be the major cause of the differences in the mechanical parameters obtained by the simulation. As shown in Tab. 3, the data of square RVEs with short CNTs were mostly in the upper or lower bound and the cylindrical RVE data were the other lower or upper bound, which was broadly consistent with the long CNT RVEs. The data from these three RVEs with short CNTs are close too. Compared with the long CNT RVEs, the deformations of the short CNT RVEs along the z-axis direction were not uniform due to the material inhomogeneity in the z-axis direction, which was caused by the fact that the length CNTs was less than that of the matrixes. Therefore, there might be a slight deviation of the selected values of displacements in the xy plane during the calculation, such as $\Delta a$ and $\Delta b$, which could lead to the differences of the Poisson's ratio and thus brought changes to other parameters.
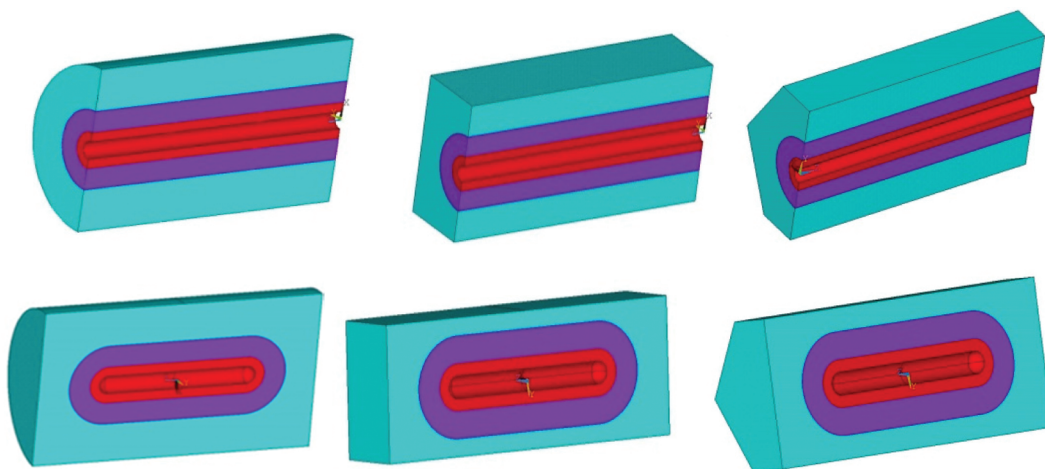


**Figure 3:** Models of six types of RVEs

**Table 2:** Material properties of long CNT RVEs obtained from simulations

| CNT vol% | RVEs | $E_z$ (GPa) | $E_x = E_y$ (GPa) | $G_{xy}$ (GPa) | $v_{zx} = v_{zy}$ | $v_{xy}$ | $v_{xz} = v_{yz}$ |
|---|---|---|---|---|---|---|---|
| | Cylinder | 10.692 | 2.474 | 0.772 | 0.398 | 0.601 | 0.092 |
| | Square | 10.692 | 2.245 | 0.683 | 0.397 | 0.643 | 0.083 |
| 1 | Hexagon | 10.692 | 2.410 | 0.747 | 0.398 | 0.613 | 0.090 |
| | Mean | 10.692 | 2.376 | 0.734 | 0.398 | 0.619 | 0.088 |
| | Deviation | 1.05% | −0.88% | −1.21% | 0 | 0.98% | −2.2% |
| | Cylinder | 19.398 | 2.921 | 0.920 | 0.396 | 0.588 | 0.060 |
| | Square | 19.399 | 2.669 | 0.817 | 0.395 | 0.634 | 0.054 |
| 2 | Hexagon | 19.399 | 2.856 | 0.892 | 0.397 | 0.601 | 0.058 |
| | Mean | 19.399 | 2.815 | 0.876 | 0.396 | 0.608 | 0.057 |
| | Deviation | 1.37% | −0.53% | −0.90% | 0 | 1.16% | −3.39% |
| | Cylinder | 28.146 | 3.582 | 1.165 | 0.394 | 0.537 | 0.050 |
| | Square | 28.147 | 3.330 | 1.049 | 0.393 | 0.588 | 0.046 |
| 3 | Hexagon | 28.147 | 3.523 | 1.135 | 0.394 | 0.552 | 0.049 |
| | Mean | 28.147 | 3.478 | 1.116 | 0.394 | 0.559 | 0.048 |
| | Deviation | 1.65% | −0.23% | −0.88% | 0 | 1.82% | −4% |
| | Cylinder | 36.935 | 4.430 | 1.510 | 0.392 | 0.467 | 0.047 |
| | Square | 36.937 | 4.199 | 1.376 | 0.390 | 0.526 | 0.044 |
| 4 | Hexagon | 36.937 | 4.386 | 1.477 | 0.392 | 0.485 | 0.047 |
| | Mean | 36.936 | 4.338 | 1.454 | 0.391 | 0.493 | 0.046 |
| | Deviation | 1.90% | 0.02% | −0.82% | −0.26% | 2.92% | −2.13% |
| | Cylinder | 45.766 | 5.430 | 1.951 | 0.390 | 0.391 | 0.046 |
| | Square | 45.768 | 5.239 | 1.797 | 0.387 | 0.458 | 0.044 |
| 5 | Hexagon | 45.768 | 5.408 | 1.916 | 0.390 | 0.411 | 0.046 |
| | Mean | 45.767 | 5.359 | 1.888 | 0.389 | 0.420 | 0.045 |
| | Deviation | 2.15% | 0.41% | −0.89% | −0.26% | 4.74% | −2.17% |

Equivalent mechanical properties of the long and short CNT RVEs with CNT volume fractions ranging from 0.2% to 5% are shown in Tabs. 4 and 5. The elastic moduli of the long and short CNT RVEs increased with increasing CNT volume fraction. The variation tendency of the longitudinal Young's modulus $E_z$ with the volume fraction of CNTs was consistent with the conclusion reported previously [49], in which a multiscale bridging model for nanocomposites was proposed. Moreover, when the volume fraction of CNTs was 5%, the value of $E_z$ of the long CNT RVEs was 45.767 GPa, which was close to the value of around 43 GPa reported previously [49]. Based on the fact that the elastic modulus of CNTs is much larger than that of the epoxy resin, the deformation of matrix is greater than that of CNTs under axial tension load, so the shear stress and shear strain appear at the interface, through which the load is reasonably distributed in the CNT and matrix. For the above reasons, the elastic modulus of two types of RVEs increases compared with the matrix. The CNT is the main component to bear the load in the long CNT RVE for the reason that it traverses the polymer matrix, so the longitudinal Young's modulus of long CNT RVE is relatively high. In contrast, due to the fact that the CNT serves as a short fiber embedded in the matrix, when a force is applied to the short CNT RVE, the CNT does not bear the load directly, which is transferred from the matrix to the CNT through the

interface. Therefore, for the same volume fraction, the longitudinal Young's modulus $E_z$ of the long CNT RVEs was greater than that of short CNT RVEs. There was little difference in $E_x$ and $E_y$ between the two kinds of RVEs, but the gap of $E_z$ increased with the increase in the CNT content. When the CNT volume fraction reached 9%, the $E_z$ value of the long CNT RVEs was around 13 times that obtained from the short CNT RVEs.

**Table 3:** Material properties of short CNT RVEs obtained from simulations

| CNT vol% | RVEs | $E_z$ (GPa) | $E_x = E_y$ (GPa) | $G_{xy}$ (GPa) | $v_{zx} = v_{zy}$ | $v_{xy}$ | $v_{xz} = v_{yz}$ |
|---|---|---|---|---|---|---|---|
| | Cylinder | 2.617 | 2.198 | 0.761 | 0.401 | 0.445 | 0.337 |
| | Square | 2.615 | 2.124 | 0.665 | 0.403 | 0.596 | 0.327 |
| 1 | Hexagon | 2.617 | 2.098 | 0.733 | 0.398 | 0.430 | 0.319 |
| | Mean | 2.616 | 2.140 | 0.720 | 0.401 | 0.490 | 0.328 |
| | Deviation | −1.62% | −0.56% | −1.77% | 1.01% | 4.70% | 1.86% |
| | Cylinder | 3.161 | 2.499 | 0.867 | 0.402 | 0.442 | 0.318 |
| | Square | 3.154 | 2.452 | 0.763 | 0.394 | 0.607 | 0.306 |
| 2 | Hexagon | 3.160 | 2.370 | 0.838 | 0.407 | 0.415 | 0.305 |
| | Mean | 3.158 | 2.440 | 0.823 | 0.401 | 0.488 | 0.310 |
| | Deviation | −2.20% | −1.49% | −3.06% | 0.75% | 6.09% | 1.31% |
| | Cylinder | 3.688 | 2.883 | 1.018 | 0.406 | 0.416 | 0.317 |
| | Square | 3.673 | 2.855 | 0.905 | 0.404 | 0.577 | 0.314 |
| 3 | Hexagon | 3.685 | 2.723 | 0.987 | 0.416 | 0.380 | 0.307 |
| | Mean | 3.682 | 2.820 | 0.970 | 0.409 | 0.458 | 0.313 |
| | Deviation | −2.26% | −2.93% | −4.34% | 2.5% | 5.77% | 1.95% |
| | Cylinder | 4.178 | 3.321 | 1.183 | 0.396 | 0.404 | 0.315 |
| | Square | 4.155 | 3.326 | 1.060 | 0.392 | 0.569 | 0.314 |
| 4 | Hexagon | 4.174 | 3.122 | 1.150 | 0.409 | 0.358 | 0.306 |
| | Mean | 4.169 | 3.256 | 1.131 | 0.399 | 0.444 | 0.312 |
| | Deviation | −1.20% | −2.57% | −4.88% | −0.25% | 9.36% | −0.64% |
| | Cylinder | 4.623 | 3.686 | 1.345 | 0.407 | 0.371 | 0.327 |
| | Square | 4.590 | 3.682 | 1.207 | 0.416 | 0.525 | 0.334 |
| 5 | Hexagon | 4.618 | 3.497 | 1.307 | 0.405 | 0.338 | 0.307 |
| | Mean | 4.610 | 3.622 | 1.286 | 0.409 | 0.411 | 0.323 |
| | Deviation | −1.54% | −3.80% | −5.30% | 2.00% | 6.20% | 0.31% |

## 3 Random Distribution Model

### 3.1 Lattice Modeling

The lattice statistical model is an important method for analyzing the macroscopic mechanical properties of reinforced composites from the microscopic scale. With a random distribution of carbon nanotubes, lattice processing is often used to deduce the macroscopic properties of the composites from the perspective of the microstructure. In this method, materials on the macroscopic scale are subdivided into cells with the same size and shape, each of which was given different physical properties to simulate the heterogeneity caused by the random distribution. From the perspective of the model's spatial structure, the orientations of the carbon nanotubes in the RVEs represented by each lattice cell were different.

**Table 4:** Equivalent mechanical properties of long CNT RVEs with volume fraction of CNTs ranging from 0.2% to 5%

| CNT vol% | $E_z$ (GPa) | $E_x = E_y$ (GPa) | $G_{xy}$ (GPa) | $v_{zx} = v_{zy}$ | $v_{xy}$ | $v_{xz} = v_{yz}$ |
|---|---|---|---|---|---|---|
| 0.2 | 3.756 | 2.135 | 0.699 | 0.400 | 0.527 | 0.227 |
| 0.4 | 5.488 | 2.202 | 0.700 | 0.399 | 0.575 | 0.160 |
| 0.6 | 7.221 | 2.257 | 0.706 | 0.399 | 0.599 | 0.125 |
| 0.8 | 8.956 | 2.314 | 0.718 | 0.398 | 0.612 | 0.103 |
| 1 | 10.692 | 2.376 | 0.734 | 0.398 | 0.619 | 0.088 |
| 1.2 | 12.430 | 2.446 | 0.755 | 0.398 | 0.622 | 0.078 |
| 1.4 | 14.170 | 2.525 | 0.779 | 0.397 | 0.622 | 0.071 |
| 1.6 | 15.911 | 2.613 | 0.807 | 0.397 | 0.619 | 0.065 |
| 1.8 | 17.654 | 2.709 | 0.840 | 0.396 | 0.614 | 0.061 |
| 2 | 19.399 | 2.815 | 0.876 | 0.396 | 0.608 | 0.057 |
| 2.2 | 21.145 | 2.931 | 0.916 | 0.395 | 0.600 | 0.055 |
| 2.4 | 22.893 | 3.055 | 0.960 | 0.395 | 0.591 | 0.053 |
| 2.6 | 24.643 | 3.187 | 1.008 | 0.395 | 0.581 | 0.051 |
| 2.8 | 26.394 | 3.329 | 1.060 | 0.394 | 0.570 | 0.049 |
| 3 | 28.147 | 3.478 | 1.116 | 0.394 | 0.559 | 0.048 |
| 3.2 | 29.901 | 3.635 | 1.176 | 0.394 | 0.546 | 0.048 |
| 3.4 | 31.657 | 3.800 | 1.240 | 0.393 | 0.533 | 0.047 |
| 3.6 | 33.415 | 3.972 | 1.307 | 0.393 | 0.520 | 0.047 |
| 3.8 | 35.175 | 4.152 | 1.379 | 0.393 | 0.507 | 0.046 |
| 4 | 36.936 | 4.338 | 1.454 | 0.391 | 0.493 | 0.046 |
| 4.2 | 38.689 | 4.529 | 1.533 | 0.391 | 0.478 | 0.046 |
| 4.4 | 40.463 | 4.729 | 1.616 | 0.391 | 0.464 | 0.046 |
| 4.6 | 42.229 | 4.932 | 1.703 | 0.390 | 0.450 | 0.045 |
| 4.8 | 43.997 | 5.143 | 1.793 | 0.390 | 0.435 | 0.045 |
| 5 | 45.767 | 5.359 | 1.888 | 0.389 | 0.420 | 0.045 |

A 3-D microscale unit cell that was discretized into cubic elements was adopted to demonstrate how the lattice model simulates the mechanical behaviors of the CNT-reinforced polymer composites, as shown in Fig. 4. The element used in the lattice model was defined by eight nodes and the orthotropic material properties. The average computed results were input into each element. A cube model with a length of 0.1 mm was established and divided into 8000 elements, and thus, each element side length was 5 $\mu$m. We randomly selected 20% of the elements to have various parameters of the long CNT RVEs in which the volume fraction varied from 0.2% to 5%. The properties of the remaining elements were the same as parameters of the short CNT RVEs. Using the finite element code to generate random numbers from $-1$ to 1 and assigning these values to direction vectors of the elements made the element unit orientation random. Through this method, the CNTs were randomly distributed in the matrix. The mechanical parameters of the RVEs with different CNT contents were integrated into a data table, and the random numbers were generated using the software. The random properties of the elements containing various CNT contents were simulated by reading the parameters from specific columns of the database table based on the random number and assigning them to elements in sequence. During the

simulation process, a uniaxial tensile load was applied on the model, and the tensile length was 0.001 mm. The stochastic direction vectors of the elements were represented by different colors, as shown in Fig. 4a. Fig. 4b shows the diverse unit material numbers corresponding to the material properties of the long and short CNT RVEs. Each unit material number is on behalf of a kind of material parameters in various RVEs. In addition, the displacement diagram and effective stress cloud chart are displayed in Figs. 4c and 4d. Fig. 4d shows that the mechanical behavior of this composite material model was uniform overall.

**Table 5:** Equivalent mechanical properties of short CNT RVEs with volume fraction of CNTs ranging from 0.2% to 5%

| CNT vol% | $E_z$ (GPa) | $E_x = E_y$ (GPa) | $G_{xy}$ (GPa) | $v_{zx} = v_{zy}$ | $v_{xy}$ | $v_{xz} = v_{yz}$ |
|---|---|---|---|---|---|---|
| 0.2 | 2.149 | 2.017 | 0.694 | 0.399 | 0.456 | 0.375 |
| 0.4 | 2.272 | 2.044 | 0.693 | 0.394 | 0.478 | 0.355 |
| 0.6 | 2.390 | 2.065 | 0.699 | 0.399 | 0.482 | 0.344 |
| 0.8 | 2.505 | 2.093 | 0.708 | 0.404 | 0.483 | 0.338 |
| 1 | 2.616 | 2.140 | 0.720 | 0.401 | 0.490 | 0.328 |
| 1.2 | 2.726 | 2.191 | 0.735 | 0.400 | 0.494 | 0.321 |
| 1.4 | 2.835 | 2.248 | 0.754 | 0.398 | 0.495 | 0.316 |
| 1.6 | 2.944 | 2.317 | 0.774 | 0.393 | 0.500 | 0.309 |
| 1.8 | 3.051 | 2.388 | 0.797 | 0.391 | 0.501 | 0.305 |
| 2 | 3.158 | 2.440 | 0.823 | 0.401 | 0.488 | 0.310 |
| 2.2 | 3.265 | 2.515 | 0.849 | 0.400 | 0.484 | 0.308 |
| 2.4 | 3.371 | 2.575 | 0.878 | 0.409 | 0.471 | 0.312 |
| 2.6 | 3.475 | 2.661 | 0.908 | 0.405 | 0.470 | 0.310 |
| 2.8 | 3.579 | 2.729 | 0.938 | 0.411 | 0.458 | 0.314 |
| 3 | 3.682 | 2.805 | 0.970 | 0.415 | 0.450 | 0.316 |
| 3.2 | 3.782 | 2.899 | 1.002 | 0.408 | 0.451 | 0.313 |
| 3.4 | 3.881 | 2.990 | 1.034 | 0.406 | 0.450 | 0.312 |
| 3.6 | 3.980 | 3.083 | 1.066 | 0.402 | 0.449 | 0.311 |
| 3.8 | 4.076 | 3.159 | 1.099 | 0.404 | 0.441 | 0.314 |
| 4 | 4.169 | 3.256 | 1.131 | 0.399 | 0.444 | 0.312 |
| 4.2 | 4.262 | 3.332 | 1.163 | 0.400 | 0.437 | 0.312 |
| 4.4 | 4.352 | 3.407 | 1.195 | 0.404 | 0.430 | 0.316 |
| 4.6 | 4.440 | 3.444 | 1.225 | 0.419 | 0.409 | 0.325 |
| 4.8 | 4.526 | 3.555 | 1.256 | 0.406 | 0.418 | 0.319 |
| 5 | 4.610 | 3.622 | 1.286 | 0.409 | 0.411 | 0.323 |

Fig. 5a shows the schematic diagram of the experimental samples for the tensile property testing of the resin casting body, which followed the State Standard of the People's Republic of China guidelines. In this study, a series of experiments were also conducted to test the CNT-reinforced composite properties, and a photograph of the test specimen is displayed in Fig. 5b. To form composites with different concentrations of CNTs, the CNTs were weighed using an electric balance based on the required mass fractions and then were added into a mixture of epoxy resin and curing agent. After being stirred well, the mixture was dispersed with an ultrasonic dispersion instrument for 4 h. After this, the dispersed liquid was poured into the mold and heated at 80°C

for 2 h in a heating cabinet. Finally, the specimen was removed from the mold after it cooled completely. The mechanical properties of the material were tested by a microcomputer-controlled electronic universal testing machine. The tensile rate was set to 2 mm/min. The test sample was clamped using a testing machine, and the central axis of the test sample was aligned with central line of the upper and lower fixtures. The experimental sample underwent continuous loading with a specified uniform speed, and failure load value was recorded when the specimen became broken.
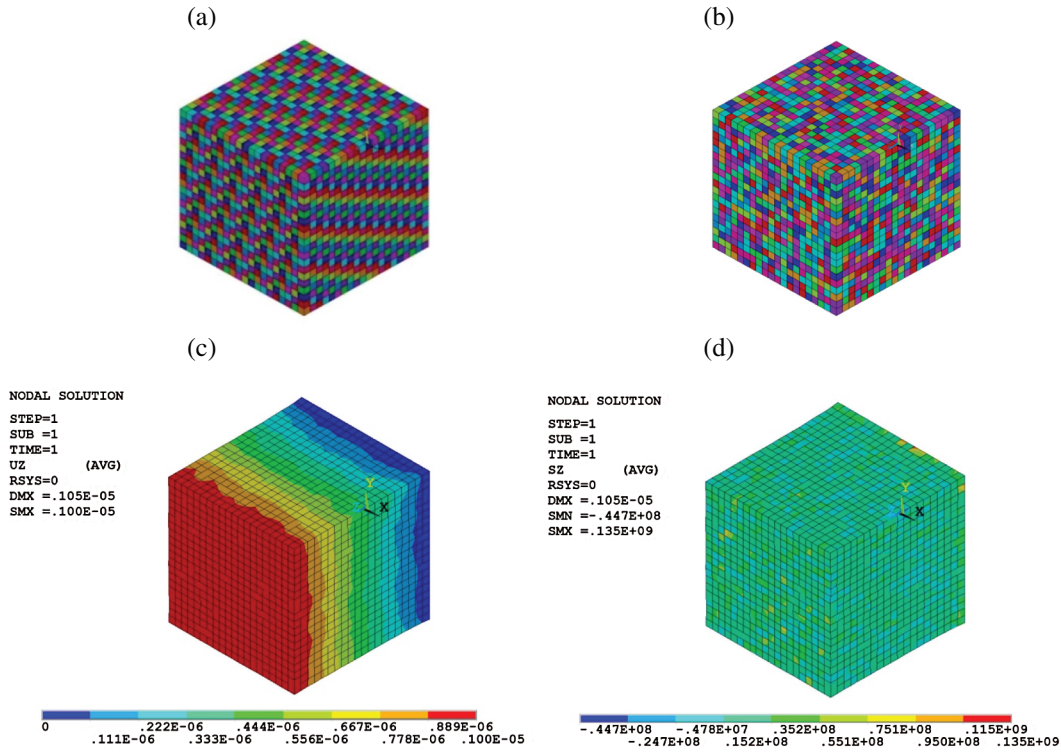


**Figure 4:** Randomly generated features for elements in a unit cell: (a) random CNT orientation represented by different colors, (b) random RVE properties represented by different colors, (c) displacement diagram, and (d) effective stress cloud chart

Because the CNTs were very small, the element dimensions in the simulation also needed to be sufficiently small, and the number of elements in the equi-volume model was very large. Cracking generally occurred in the centers of the specimens in the experiments. Thus, the middle region was selected to simulate the tensile fracture process. To reduce the computational complexity, the model was scaled down to 10%, i.e., the length, width and height were 5, 0.4, and 1 mm, respectively. The side length of each element was 20 $\mu$m. The CNT contents were varied at 0.2% intervals. The models with random CNT orientation vectors and element properties indicated by color are shown in Fig. 6. The conversion relation between volume fraction and mass fraction is as follows:

$$wt\% = \frac{\rho_{\text{CNT}} \sum vol_i\%}{\rho_{\text{CNT}} \sum vol_i\% + \rho_{\text{epoxy}}(1 - \sum vol_i\%)} \tag{11}$$

where *wt*% is the mass fraction of the composite model, $vol_i$% is the volume content of the CNTs in each element, $\rho_{CNT}$ is the density of the CNTs, and $\rho_{epoxy}$ is the density of the epoxy.
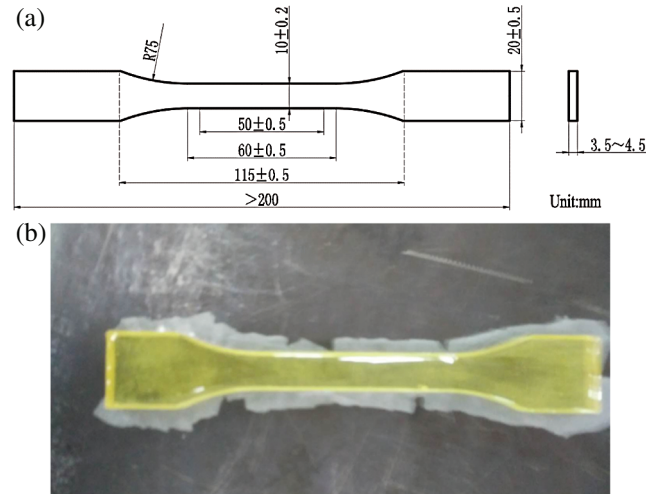


**Figure 5:** Experimental samples: (a) schematic diagram of the samples used in the experiments and (b) photograph of the test specimen used in the experiments
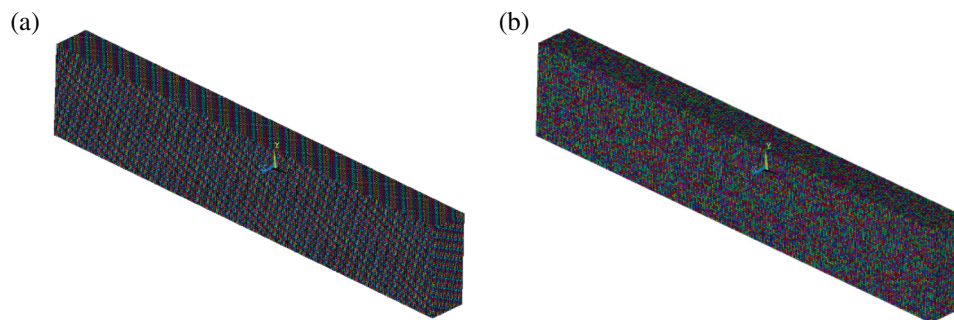


**Figure 6:** (a) Random CNT orientation represented by different colors and (b) random elements properties represented by different colors

To obtain the tensile properties of the finite element model, a uniaxial tension was exerted on the model, and the tensile length was 0.01 mm. The tensile modulus and Poisson's ratio were calculated using Eqs. (4) and (6). For the tensile fracture process of the CNT-reinforced composites, the step loading was exerted on the model with the strength limit of the elements set, and the stress-strain curves were obtained. In a unified deformation field, except for the reasons of the stress concentration caused by the structural factors, the main cause of the microfracture is the inhomogeneity of physical properties of the mesoscopic units. In this paper, the equivalent stress $\bar{\sigma}$, also known as Von Mises stress which can be calculated by the finite element software,

was employed to judge the failure of the elements in the model, and its calculation formula can be written as

$$\overline{\sigma} = \frac{1}{\sqrt{2}}\sqrt{(\sigma_x - \sigma_y)^2 + (\sigma_y - \sigma_z)^2 + (\sigma_z - \sigma_x)^2 + 6(\tau_{xy}^2 + \tau_{yz}^2 + \tau_{zx}^2)} \qquad (12)$$

where $\sigma_x$, $\sigma_y$ and $\sigma_z$ are the axial stresses in the x, y and z directions, and $\tau_{xy}$, $\tau_{yz}$ and $\tau_{zx}$ are the shear stresses in the xy, yz and zx planes respectively. Relevant calculation programs were written to simulate the tensile deformation and failure procedure of the models. During the course of the simulation, the strength limit for the element was set first, and then the axial displacement was applied on one end of the model step by step. The elements whose equivalent stress exceeded the strength limit were extracted and killed at each loading step, and then the next round of calculations was preceded according to the program, until the material was completely destroyed. Furthermore, the force acting on the sample under the loading step was output.

### 3.2 Results and Discussion

Using the material parameters of the RVEs in which the CNT volume fraction varied from 0.2% to 2% as input data, the mechanical properties of the composite material with the CNT mass fraction of 1.6% (i.e., CNT volume fraction of 1.1%) were obtained, as illustrated in Tab. 6. If the content of CNTs was certain, the tensile modulus of the CNT-reinforced polymer was basically stable. For the case of 1.63 wt% (1.1 vol%) CNTs in the epoxy matrix, the tensile modulus was around 2.622 GPa, which was very close to the simulation result of about 2.63 GPa reported previously [18], and the Poisson's ratio varied between 0.37 and 0.42. The stress-strain curve obtained from the simulation for the failure process of the CNT-reinforced composites is also presented in Fig. 7. The tensile strength and elongation at break were 38.65 MPa and 1.67%, respectively, as determined from Fig. 7. The curve was linear in the initial stage, but nonlinear deformation occurred with the increase in the loading force. Moreover, the slope of the curve in the linear stage was roughly equal to the value of the Young's modulus in Tab. 6, which also confirmed the reliability of the two methods that were used to calculate the mechanical parameters and to simulate the fracture process, respectively. During the course of the simulation, the programs output figures showing the deformation states at every step after loading.

**Table 6:** Mechanical parameters of composites with the CNT mass fraction of 1.6%

| wt% | vol% | Tensile modulus (GPa) | Poisson's ratio $v$ |
|-----|------|----------------------|---------------------|
| 1.633 | 1.095 | 2.622 | 0.368 |
| 1.631 | 1.093 | 2.622 | 0.387 |
| 1.633 | 1.095 | 2.622 | 0.422 |
| 1.632 | 1.094 | 2.622 | 0.416 |

Tab. 7 shows the physical performances of the CNT-reinforced polymer composites containing 1.2% CNTs by mass. The tensile modulus reached 2.5 GPa, which was coincident with the predicted value of around 2.47 GPa reported previously [18], and the Poisson's ratio was in the range from 0.38 to 0.45. By means of simulation analysis, the stress-strain curve was also obtained, as shown in Fig. 8. Fig. 8 shows that the tensile strength and elongation at break were 39.15 MPa and 1.8%, respectively. There were a set of experiments conducted to test the tensile performances of the CNT-reinforced epoxy composites, and the experimental results for

composites containing 1% CNTs are plotted in Fig. 8. We found some differences between the simulation and experimental results, which may have been caused by the inhomogeneity of the real materials. Because agglomeration and bending of the CNTs in the experimental specimens emerged inevitably, there were defects in the material, and the properties of two samples could not be identical. The moduli calculated by the equations and the slopes of stress-strain curves were compared for composites containing 1.6% CNTs. The slopes of the curves in the linear stage agreed with the values of the Young's modulus in Tab. 7.
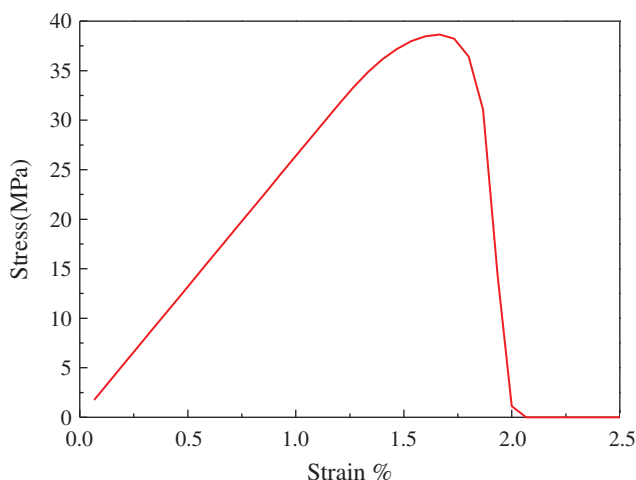


**Figure 7:** Stress-strain curve obtained by simulating the failure process of the CNT-reinforced composites with a CNT mass fraction of 1.6%

**Table 7:** Mechanical parameters of the composite material with a CNT mass fraction of 1.2%

| wt% | vol% | Tensile modulus (GPa) | Poisson's ratio $\nu$ |
|---|---|---|---|
| 1.187 | 0.795 | 2.5 | 0.456 |
| 1.186 | 0.794 | 2.5 | 0.388 |
| 1.185 | 0.793 | 2.5 | 0.382 |
| 1.185 | 0.793 | 2.5 | 0.384 |

When the CNT mass fraction of the composites was 2.2%, the tensile characteristic values are shown in Tab. 8. The tensile modulus was approximately 2.8 GPa, and the Poisson's ratio varied from 0.36 to 0.39, which were determined by analyzing the data in Tab. 8. The stress-strain curve extracted from the simulation results is plotted in Fig. 9, from which it can be seen that the tensile strength and elongation at break were 37.67 MPa and 1.53%, respectively.

A series of experiments that aimed to examine the tensile properties of the CNT-reinforced composites was also performed. The experimental results for complex materials that included 2% CNTs are displayed in Fig. 9. There was good agreement between the simulation results and the experiments in terms of the slopes of the curves. However, the differences between the values were slightly large, which may have also resulted from the increase in the number of defects and holes in the material samples with increasing CNT fraction. Like the other two materials whose CNT

contents were 1.2% and 1.6%, the stress-strain ratio in the linear phase agreed with the value of the tensile modulus in Tab. 8. The fracture process images of the CNT-reinforced composites with a CNT mass fraction of 1.6% are presented in Fig. 10. The failure procedure underwent stages of crack initiation and propagation.
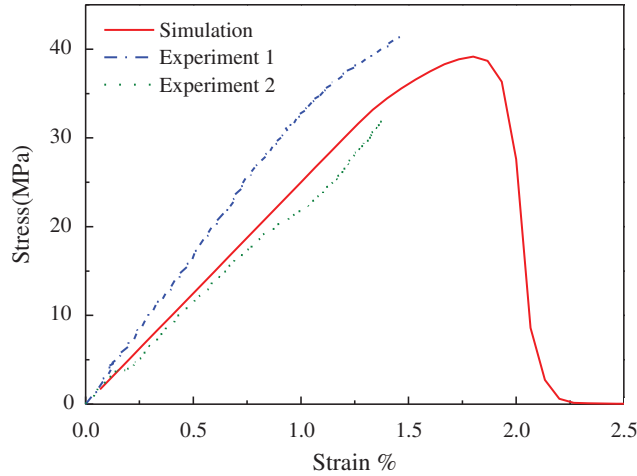


**Figure 8:** Simulation and experimental results of the CNT-reinforced composites with a CNT mass fraction of 1.2%

**Table 8:** Mechanical parameters of the composite materials with a CNT mass fraction of 2.2%

| wt% | vol% | Tensile modulus (GPa) | Poisson's ratio $v$ |
| --- | --- | --- | --- |
| 2.23 | 1.5 | 2.812 | 0.379 |
| 2.226 | 1.5 | 2.81 | 0.371 |
| 2.228 | 1.5 | 2.813 | 0.364 |
| 2.229 | 1.5 | 2.811 | 0.393 |

Fig. 11 shows a comparison of the composites with different mass contents. It is noticeable that the mass fraction of the CNTs had obvious influence on the tensile properties of the materials. As the mass fraction of CNTs increased, the Young modulus of the simulated material increased, and the corresponding slope of the stress-strain curve increased, which agrees with the variation trend of the modulus with the CNT content presented previously [17,33]. The research methods used in reference [17,33] were an MD simulation method and a large-scale hybrid Monte-Carlo FEA simulation, respectively. The specific values of the Young modulus of the composites with the same contents of CNTs were different between the references and this work due to the different parameters of the CNTs, epoxy matrix, and interface selected in these studies. On the contrary, the fracture elongation and the strength decreased, which is in agreement with the conclusion in reference [50]. Zhang et al. [50] produced CNT-reinforced epoxy composites using methods of ultrasonic dispersion and mold casting surface treatment. They also conducted tensile and bending tests on the prepared composites to obtain the relationship between the CNT contents and the material performance. Their results showed that when the mass fraction was between 0.5% and 2.0%, the tensile strength and elongation at break decreased with increasing

CNT contents. However, the elongation at break and tensile strength calculated by the finite element method in this paper were lower than those reported in reference [50]. In the preparation of materials, Zhang et al. treated the surfaces of the CNTs with nitric acid boiling by point reflux method, but there was no prior treatment for the CNTs in this study, which may have been the reason for the deviations between the two studies. The CNTs are arranged out of order in the direction of tension. In addition, the function of matrix in composites is to make the CNTs bond together and keep them in relative position, which can help the CNTs enhance the matrix collaboratively. For these reasons, there is a positive correlation between the enhancement function of CNTs on matrix and the mass fractions of CNTs within a certain range. However, when the CNT contents is relatively high, the defects in composites increase, which leads to the decrease of tensile strength.
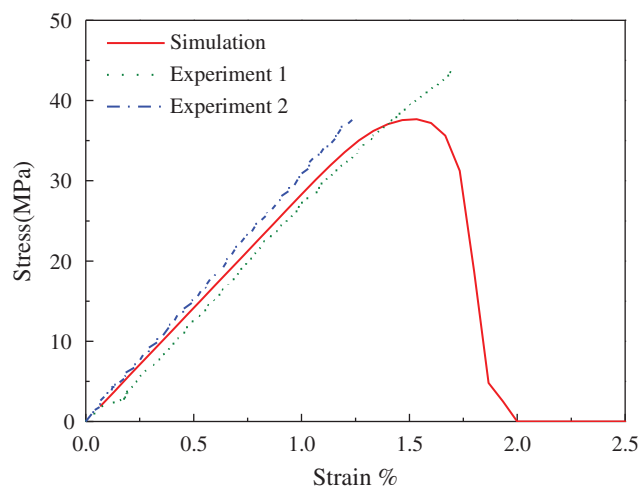


**Figure 9:** Simulation and experimental results of the CNT-reinforced composites with a CNT mass fraction of 2.2%
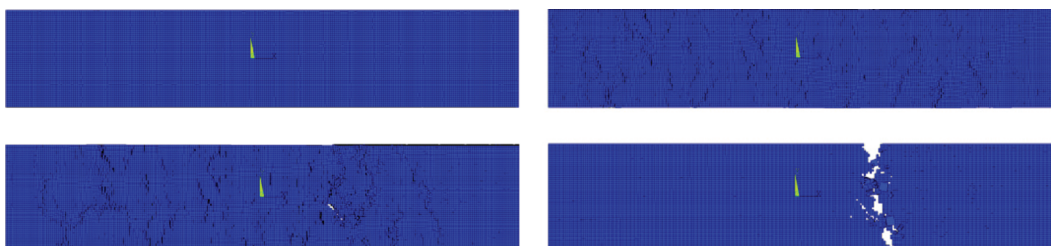


**Figure 10:** Tensile fracture process diagram obtained from simulating the failure process of the CNT-reinforced composites with a CNT mass fraction of 2.2%

## 4 Modeling of CNT-Reinforced Gradient Composites

The FG-CNTRC model was also studied, and five distributions of CNTs along the model thickness direction were considered: random, V-shaped, W-shaped, X-shaped, and O-shaped distributions, which were represented by FG-U, FG-V, FG-W, FG-X, and FG-O, respectively. Fig. 12

shows the cross-sections of the models with various distributions. The random distribution can be regarded as a uniform distribution from a macroscopic perspective. Both models with random distributions of carbon nanotubes and other distribution forms had the same volume fraction of carbon nanotubes, which was about 2.6%, i.e., the mass percent of CNTs was 3.8%.
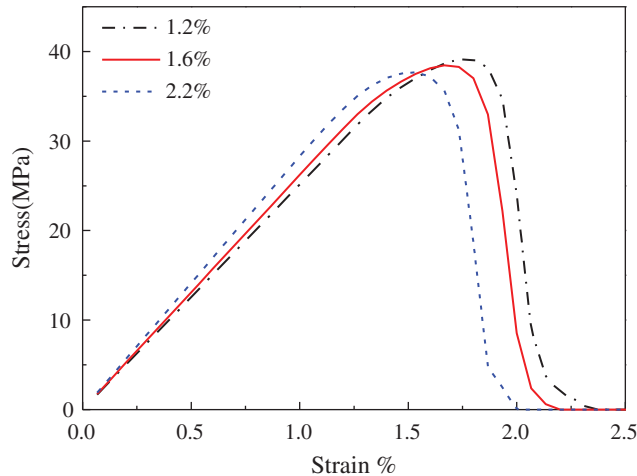


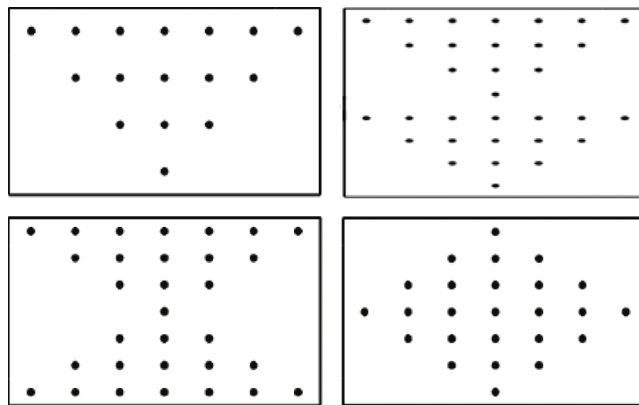**Figure 11:** Comparison of composites with different mass contents



**Figure 12:** Four forms of CNT-enhanced gradient composites (FG-V, FG-VV, FG-X, and FG-O)

The finite element models of the CNT-reinforced epoxy resin composites with five types were established. The size of each distributed model was the same, with dimensions of 5 mm × 1 mm × 0.4 mm. First, the representative volume element (RVE) model in the paper was used to calculate the mechanical property parameters of the RVEs with different CNT contents. The FG-CNTRC model was divided equally into several layers along the thickness direction. Considering the relationship between the properties of the FG-CNTRC and the distribution forms, the discrete layer elements were endowed with the physical parameters of the RVEs with different CNT contents to simulate the variation characteristics of the material parameters along the thickness direction. Fig. 13 shows the finite element model of the V-shaped distribution gradient composite,

in which the different colors represent different RVE material parameters. Fig. 13 shows that the established model was representative of graded materials. The CNT contents in the same layer were the same, but the forms of the CNTs in the RVEs included penetrating and embedding types, so each layer contained two kinds of material parameters.
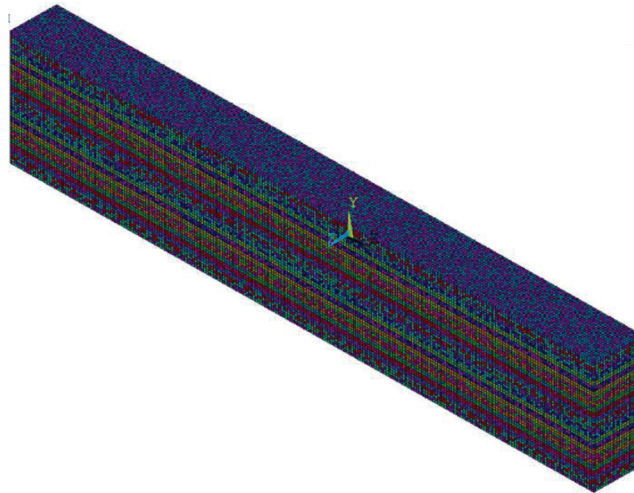


**Figure 13:** V-shaped distributed laminate finite element model

### 4.1 Tensile Properties of CNT-Reinforced Gradient Materials

To calculate the tensile moduli and Poisson's ratios of the CNT-reinforced gradient materials, each finite element model was stretched axially. The elastic modulus and Poisson's ratio of the tensile direction were calculated using Eqs. (4) and (6). Fig. 14 shows the stress distribution diagrams of the FG-V, FG-W, FG-X, and FG-O materials. It should be noted that unlike the FG-U material in which the stress was uniformly distributed, stresses in four types of gradient composites were significantly influenced by the compositional gradient and corresponding variations in modulus of elasticity across the thickness. This is because of dependency of stress on both position and properties variations across the thickness in inhomogeneous materials. The stress of the V-shaped distribution exhibited a graded distribution, and the stress value of the upper part of the model, i.e., the part with a higher CNT content, was greater than that of the lower part of the model. The stress cloud diagram of the FG-W model showed that the stress increased from the bottom to the middle and then a sudden increase occurred later. Similarly, the X- and O-shaped distributions exhibited the same behavior, that is, the stress distributions were consistent with the CNT content gradients. It is interesting to note that, on the whole, through-the-thickness stress distribution was symmetrical in FG-O and FG-X materials due to symmetry in composition across the thickness, whereas FG-W and FG-V composites showed asymmetrical distribution. Tab. 9 shows the tensile modulus and Poisson's ratio of the five kinds of materials obtained by the simulations. The data show that there was not much difference between the tensile moduli of these materials. Furthermore, the tensile modulus of the FG-O material was the largest, the tensile modulus of the FG-U composite was the smallest, and the graded distributions could be sorted based on the elastic modulus in the order of FG-O > FG-X > FG-V > FG-W > FG-U. Tab. 10 shows the mechanical parameters of the X-shaped graded models with different CNT

volume fractions. Tab. 10 shows that the tensile modulus increased as the CNT content increased, but the change in the Poisson's ratio had no evident pattern.

During the simulation of the tensile failure process of the gradient materials, the method of birth-death element was also adopted, and the equivalent stress $\bar{\sigma}$ of each element in the model was used to judge the failure of each element by comparing $\bar{\sigma}$ with the set strength limit as well. Tab. 9 also shows the tensile strength of the five forms of the material models. The simulated results showed that the tensile strengths of the four types of the graded composites had little difference. However, the strength of the FG-U was much larger than that of the other composites with gradient distributions, which is shown in Fig. 15. The tensile strength of the U-shaped material model was about 34 MPa, whereas the limiting stress of the four kinds of graded composites was approximately 30–31 MPa. In the initial stage of each stress-strain curve, the stress increased linearly with the increase in strain, and the slope corresponded to the tensile modulus.
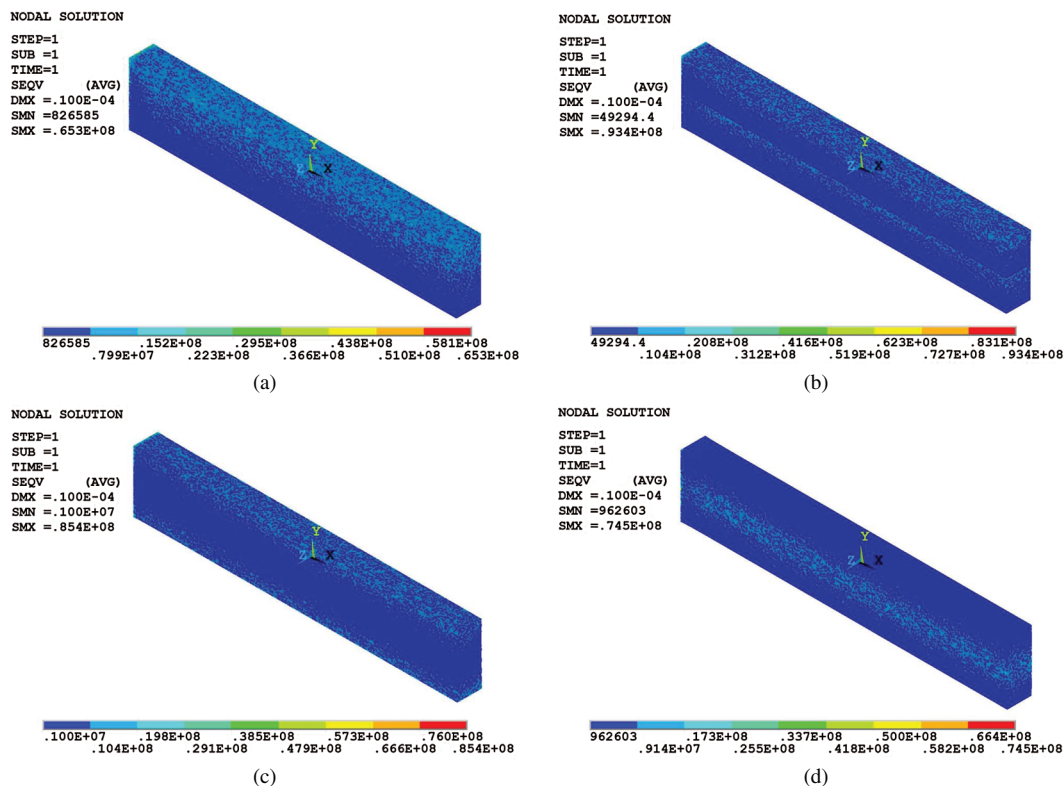


**Figure 14:** Stress distribution figures of the graded composites: (a) FG-V, (b) FG-W, (c) FG-X and (d) FG-O

### 4.1.1 Bending Properties of CNT-Reinforced Gradient Materials

In this study, finite element software was used to simulate the three-point bending process of CNT-reinforced graded composite materials, and the bending moduli of the gradient composite materials were obtained. Fig. 16 shows the three-point bending displacement cloud diagram of the X-shaped-distributed graded material. According to the theories of mechanics of materials,

the bending modulus $E_w$ of the structures in three-point bending test can be calculated by

$$E_w = \frac{FL_1^3}{48I\Delta L_1} \tag{13}$$

where $F$ is the force exerted on the middle of the upper surface of the structure, $L_1$ is the span of two supports, $\Delta L_1$ is the deflection of the specimen at mid-span, and $I = \frac{bh^3}{12}$ is the moment of inertia of the structure with the rectangular section, in which $b$ and $h$ denote the width and height of the model respectively.

**Table 9:** Tensile properties in different distributions

| Distribution pattern | Tensile modulus (GPa) | Poisson's ratio $v$ | Tensile strength (MPa) |
|---|---|---|---|
| FG-V | 3.516 | 0.425 | 30.82 |
| FG-W | 3.491 | 0.402 | 30.32 |
| FG-X | 3.517 | 0.329 | 30.57 |
| FG-O | 3.526 | 0.38 | 30.52 |
| FG-U | 3.453 | 0.385 | 34.17 |

**Table 10:** Mechanical parameters of X-shaped gradient models with different CNT volume fractions

| FG-X | Tensile modulus (GPa) | Poisson's ratio $v$ |
|---|---|---|
| 0.6% | 2.367 | 0.434 |
| 1.6% | 2.868 | 0.440 |
| 2.1% | 3.177 | 0.436 |
| 2.6% | 3.517 | 0.329 |

As shown in Tab. 11, the order of the bending moduli of the materials was FG-X > FG-U > FG-W > FG-V > FG-O. Among the five types of materials, the maximum values of the bending modulus occurred for the FG-X composites. It was concluded that CNTs distributed near the top and bottom sides were more efficient at enhancing the bending moduli of the materials than the CNTs distributed close to the center section. In general, the modulus of the material is corresponding to structural stiffness, which has an inverse relationship with the deflection of the structure. Gao et al. [51] extracted the displacement of the intermediate node by exerting a uniform pressure on the upper surface of the CNT-reinforced functionally graded plate. The results showed that, when the volume fraction of the CNTs was the same, the order of the distribution modes in terms of the structural stiffness was FG-X > FG-U > FG-V > FG-O. In comparison, the results in the reference were consistent with the three-point bending simulation results in this paper. As Tab. 12 shows, the bending moduli of the X-shaped gradient composites became larger as the CNT volume fraction increased from 0.6% to 2.6% for the FG-X materials. This also suggested that the stiffness of the graded material models tended to be higher when the CNT volume fraction increased. Zhang et al. [52] carried out the analysis of the nonlinear bending behaviors of FG-CNTRC thick plates using the element-free improved moving least-squares Ritz method. The research results showed that the deflection of the plates decreased when

the CNT volume fraction increased from 0.11 to 0.17. That is, the stiffness of the gradient plates was improved with increasing the CNT contents. For different types of FG-CNTRC plates with the same mass fraction of CNTs, the FG-O and FG-V plates had comparatively larger values of the non-dimensional central deflection, while the FG-U and FG-X plates had smaller deflections, which agreed with the conclusions of this paper.
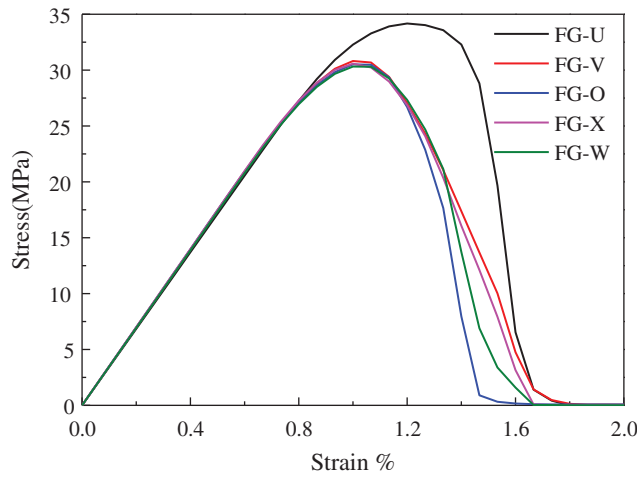


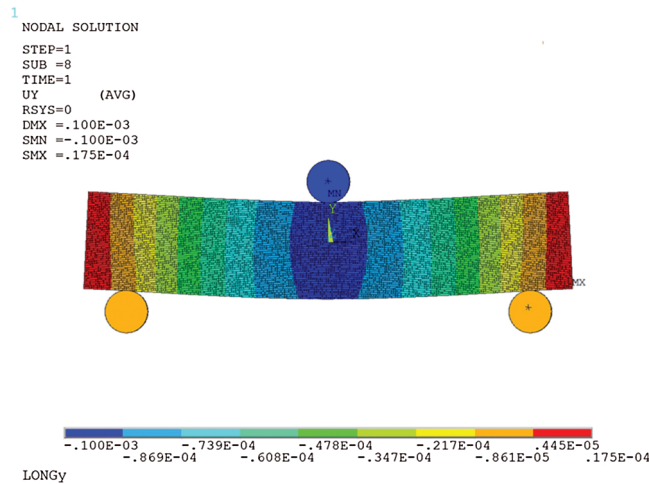**Figure 15:** Stress-strain curves of FG-V, FG-W, FG-X, and FG-O under tensile loads



**Figure 16:** Three-point bending displacement cloud diagram of FG-X

Moreover, based on the material mechanics, the calculating formula of the flexure strength $\sigma_f$ in the three-point bending test can be expressed as

$$\sigma_f = \frac{3F_{max}L_1}{2bh^2} \tag{14}$$

where $F_{max}$ is the fracture load of the specimen. In the process of the bending failure simulation, the displacement was exerted on the squeeze head using the step loading method, and then the load was transferred to the model. In the simulation of three-point bending fracture, the maximum tensile-stress criterion was used to judge the failure of each element in the specimens. After each loading, the tensile stress of each element in the model was compared with the set maximum tensile stress, and the elements whose stresses increased to the set value were killed. Finally, the force of reaction and displacement of the squeeze head were extracted using programs. The simulation results of the bending strengths are shown in Tab. 11. The ultimate flexural strength of the model with the FG-V distribution was the largest, and the X-shaped graded material had the minimum bending strength of all the materials with different distribution forms. The order of the maximal flexural strengths of the gradient composites was FG-V > FG-W > FG-O > FG-U > FG-X. This is because the profile of the reinforcement distribution affects the bending strength of the composites. This phenomenon highlights the advantage of FG-CNTRC, in which a desired bending strength can be achieved by adjusting the distribution of CNTs along the thickness direction of the composites. It can be concluded that the CNTs distributed in order of increasing contents from bottom to top induce higher strength values of the FG-CNTRC.

**Table 11:** Bending performance in different distributions

| Distribution pattern | Bending modulus (GPa) | Bending strength (MPa) |
|---|---|---|
| FG-V | 2.6815 | 92.60 |
| FG-W | 2.7103 | 88.25 |
| FG-X | 3.2130 | 59.48 |
| FG-O | 2.2745 | 81.25 |
| FG-U | 2.7662 | 72.48 |

**Table 12:** Bending modulus of X-shaped gradient models with different CNT volume fractions

| FG-X | Bending modulus (GPa) |
|---|---|
| 0.6% | 1.9650 |
| 1.6% | 2.5231 |
| 2.1% | 2.8348 |
| 2.6% | 3.2130 |

## 5 Conclusions

In this paper, multi-scale finite element modeling of carbon-nanotube-reinforced polymer composites from micro- to macro-scale was carried out. The effective mechanical properties of the CNT-reinforced composites and FG-CNTRCs were predicted based on models with different dimensions. The conclusions can be summarized as follows.

(1) The models of the prismatic RVEs with circular, square, and hexagonal cross sections were established to represent nanocomposites that contained long or short CNTs. A finite element program was written to simulate the modeling and loading procedure of the RVEs, and the mechanical properties of the nanocomposites with various volume fractions of

CNTs were extracted through the procedure, which can be used directly in the macroscopic research of the nanocomposites. The results showed that the elastic moduli of the long and short CNT RVEs increased with increasing CNT volume fraction, and for the same volume fraction, the longitudinal Young's modulus $E_z$ of the long CNT RVEs was greater than that of short CNT RVEs.

(2) A lattice statistical model was used to analyze the macroscopic mechanical properties of the reinforced composites from the microscopic scale. The tensile modulus, Poisson's ratio, and tensile strength were obtained. By comparing the simulated results and experimental data, it was found that the numerical results of the stress-strain curves were basically in agreement with the experimental data. The Young's moduli of the composites increased with increasing CNT mass fraction, but the elongation at break and the strength decreased.

(3) The graded distributions were sorted based on the tensile modulus, and the order was FG-O > FG-X > FG-V > FG-W > FG-U. The tensile strengths of the four types of graded composites had little difference, but the strength of the FG-U was much larger than those of the other composites with gradient distributions. The distribution modes were ranked by the bending stiffness, which were in the order of FG-X > FG-U > FG-V > FG-O, and the maximum flexural strengths of the gradient composites were in the order of FG-V > FG-W > FG-O > FG-U > FG-X. According to the results, it can be found that the materials with required mechanical properties can be produced by adjusting the distribution of CNTs along the thickness direction of the composites.

**Conflicts of Interest:** The authors declare that they have no conflicts of interest to report regarding the present study.

## References

1. Lijima, S. (1991). Helical microtubules of graphitic carbon. *Nature, 354(6348),* 56–58. DOI 10.1038/354056a0.
2. Giannopoulos, G. I., Kakavas, P. A., Anifantis, N. K. (2008). Evaluation of the effective mechanical properties of single walled carbon nanotubes using a spring based finite element approach. *Computational Materials Science, 41(4),* 561–569. DOI 10.1016/j.commatsci.2007.05.016.
3. Brischetto, S. (2015). A continuum shell model including van der Waals interaction for free vibrations of double-walled carbon nanotubes. *Computer Modeling in Engineering & Sciences, 104(4),* 305–327.
4. Meo, M., Rossi, M. (2007). A molecular-mechanics based finite element model for strength prediction of single wall carbon nanotubes. *Materials Science and Engineering: A, 454–455,* 170–177. DOI 10.1016/j.msea.2006.11.158.
5. Wang, X. Y., Wang, X. (2004). Numerical simulation for bending modulus of carbon nanotubes and some explanations for experiment. *Composites Part B: Engineering, 35(2),* 79–86. DOI 10.1016/S1359-8368(03)00084-2.

6. Chang, T., Gao, H. (2003). Size-dependent elastic properties of a single-walled carbon nanotube via a molecular mechanics model. *Journal of the Mechanics and Physics of Solids, 51(6),* 1059–1074. DOI 10.1016/S0022-5096(03)00006-1.

7. Niu, C., Sichel, E. K., Hoch, R., Moy, D., Tennent, H. (1997). High power electrochemical capacitors based on carbon nanotube electrodes. *Applied Physics Letters, 70(11),* 1480–1482. DOI 10.1063/1.118568.

8. Imani Yengejeh, S., Kazemi, S. A., Öchsner, A. (2016). Advances in mechanical analysis of structurally and atomically modified carbon nanotubes and degenerated nanostructures: a review. *Composites Part B: Engineering, 86,* 95–107. DOI 10.1016/j.compositesb.2015.10.006.

9. Imani Yengejeh, S., Akbar Zadeh, M., Öchsner, A. (2014). Numerical modeling of eigenmodes and eigenfrequencies of hetero-junction carbon nanotubes with pentagon–heptagon pair defects. *Computational Materials Science, 92,* 76–83. DOI 10.1016/j.commatsci.2014.05.015.

10. Hassanzadeh Aghdam, M. K., Mahmoodi, M. J. (2017). A comprehensive analysis of mechanical characteristics of carbon nanotube-metal matrix nanocomposites. *Materials Science and Engineering: A, 701,* 34–44. DOI 10.1016/j.msea.2017.06.066.

11. Zghal, S., Frikha, A., Dammak, F. (2017). Static analysis of functionally graded carbon nanotube-reinforced plate and shell structures. *Composite Structures, 176,* 1107–1123. DOI 10.1016/j.compstruct.2017.06.015.

12. Pandey, G., Thostenson, E. T. (2012). Carbon nanotube-based multifunctional polymer nanocomposites. *Polymer Reviews, 52(3–4),* 355–416. DOI 10.1080/15583724.2012.703747.

13. Lau, K., Gu, C., Hui, D. (2006). A critical review on nanotube and nanotube/nanoclay related polymer composite materials. *Composites Part B: Engineering, 37(6),* 425–436. DOI 10.1016/j.compositesb.2006.02.020.

14. Thostenson, E. T., Ren, Z., Chou, T. (2001). Advances in the science and technology of carbon nanotubes and their composites: a review. *Composites Science and Technology, 61(13),* 1899–1912. DOI 10.1016/S0266-3538(01)00094-X.

15. Sharma, S., Chandra, R., Kumar, P., Kumar, N. (2015). Thermo-mechanical characterization of multi-walled carbon nanotube reinforced polycarbonate composites: a molecular dynamics approach. *Comptes Rendus Mecanique, 343(5–6),* 371–396. DOI 10.1016/j.crme.2015.03.002.

16. Chawla, R., Sharma, S. (2017). Molecular dynamics simulation of carbon nanotube pull-out from polyethylene matrix. *Composites Science and Technology, 144,* 169–177. DOI 10.1016/j.compscitech.2017.03.029.

17. Alian, A. R., Kundalwal, S. I., Meguid, S. A. (2015). Multiscale modeling of carbon nanotube epoxy composites. *Polymer, 70,* 149–160. DOI 10.1016/j.polymer.2015.06.004.

18. Hu, Z., Arefin, M. R. H., Yan, X., Fan, Q. H. (2014). Mechanical property characterization of carbon nanotube modified polymeric nanocomposites by computer modeling. *Composites Part B: Engineering, 56,* 100–108. DOI 10.1016/j.compositesb.2013.08.052.

19. Parsapour, H., Ajori, S., Ansari, R., Haghighi, S. (2019). Tensile characteristics of single-walled carbon nanotubes endohedrally decorated with gold nanowires: a molecular dynamics study. *Diamond and Related Materials, 92,* 117–129. DOI 10.1016/j.diamond.2018.12.014.

20. Ansari, R., Ajori, S., Rouhi, S. (2015). Elastic properties and buckling behavior of single-walled carbon nanotubes functionalized with diethyltoluenediamines using molecular dynamics simulations. *Superlattices and Microstructures, 77,* 54–63. DOI 10.1016/j.spmi.2014.11.002.

21. Ajori, S., Ameri, A., Ansari, R. (2019). On the mechanical stability and buckling analysis of carbon nanotubes filled with ice nanotubes in the aqueous environment: a molecular dynamics simulation approach. *Journal of Molecular Graphics and Modelling, 89,* 74–81. DOI 10.1016/j.jmgm.2019.03.002.

22. Boroushak, S. H., Ansari, R., Ajori, S. (2018). Molecular dynamics simulations of the thermal conductivity of cross-linked functionalized single- and double-walled carbon nanotubes with polyethylene chains. *Diamond and Related Materials, 86,* 173–178. DOI 10.1016/j.diamond.2018.04.023.

23. Ansari, R., Ajori, S., Arash, B. (2012). Vibrations of single- and double-walled carbon nanotubes with layerwise boundary conditions: a molecular dynamics study. *Current Applied Physics, 12(3),* 707–711. DOI 10.1016/j.cap.2011.10.007.

24. Ajori, S., Ansari, R., Darvizeh, M. (2015). Vibration characteristics of single- and double-walled carbon nanotubes functionalized with amide and amine groups. *Physica B: Condensed Matter, 462,* 8–14. DOI 10.1016/j.physb.2015.01.003.

25. Djoudi, H., Gelin, J. C., Barrière, T. (2015). Experiments and FE simulation for twin screw mixing of nanocomposite of polypropylene/multi-walled carbon nanotubes. *Composites Science and Technology, 107,* 169–176. DOI 10.1016/j.compscitech.2014.12.017.

26. El Moumen, A., Tarfaoui, M., Lafdi, K. (2017). Mechanical characterization of carbon nanotubes based polymer composites using indentation tests. *Composites Part B: Engineering, 114,* 1–7. DOI 10.1016/j.compositesb.2017.02.005.

27. Ahmadi, M., Ansari, R., Rouhi, H. (2017). Multi-scale bending, buckling and vibration analyses of carbon fiber/carbon nanotube-reinforced polymer nanocomposite plates with various shapes. *Physica E: Low-Dimensional Systems and Nanostructures, 93,* 17–25. DOI 10.1016/j.physe.2017.05.009.

28. Khani, N., Yildiz, M., Koc, B. (2016). Elastic properties of coiled carbon nanotube reinforced nanocomposite: a finite element study. *Materials & Design, 109,* 123–132. DOI 10.1016/j.matdes.2016.06.126.

29. Zuberi, M. J. S., Esat, V. (2015). Investigating the mechanical properties of single walled carbon nanotube reinforced epoxy composite through finite element modelling. *Composites Part B: Engineering, 71,* 1–9. DOI 10.1016/j.compositesb.2014.11.020.

30. Joshi, P., Upadhyay, S. H. (2014). Evaluation of elastic properties of multi walled carbon nanotube reinforced composite. *Computational Materials Science, 81,* 332–338. DOI 10.1016/j.commatsci.2013.08.034.

31. Eslami Afrooz, I., Öchsner, A., Rahmandoust, M. (2012). Effects of the carbon nanotube distribution on the macroscopic stiffness of composite materials. *Computational Materials Science, 51(1),* 422–429. DOI 10.1016/j.commatsci.2011.08.003.

32. Chan, L. Y., Andrawes, B. (2010). Finite element analysis of carbon nanotube/cement composite with degraded bond strength. *Computational Materials Science, 47(4),* 994–1004. DOI 10.1016/j.commatsci.2009.11.035.

33. Wernik, J. M., Meguid, S. A. (2014). Multiscale micromechanical modeling of the constitutive response of carbon nanotube-reinforced structural adhesives. *International Journal of Solids and Structures, 51(14),* 2575–2589. DOI 10.1016/j.ijsolstr.2014.03.009.

34. Gupta, A. K., Harsha, S. P. (2016). Analysis of mechanical properties of carbon nanotube reinforced polymer composites using multi-scale finite element modeling approach. *Composites Part B: Engineering, 95,* 172–178. DOI 10.1016/j.compositesb.2016.04.005.

35. Grabowski, K., Zbyrad, P., Uhl, T., Staszewski, W. J., Packo, P. (2017). Multiscale electro-mechanical modeling of carbon nanotube composites. *Computational Materials Science, 135,* 169–180. DOI 10.1016/j.commatsci.2017.04.019.

36. Palacios, J. A., Ganesan, R. (2019). Dynamic response of carbon-nanotube-reinforced-polymer materials based on multiscale finite element analysis. *Composites Part B: Engineering, 166,* 497–508. DOI 10.1016/j.compositesb.2019.02.039.

37. Palacios, J. A., Ganesan, R. (2019). Reliability evaluation of carbon-nanotube-reinforced-polymer composites based on multiscale finite element model. *Composite Structures, 229,* 111381. DOI 10.1016/j.compstruct.2019.111381.

38. Feldman, E., Aboudi, J. (1997). Buckling analysis of functionally graded plates subjected to uniaxial loading. *Composite Structures, 38(1),* 29–36. DOI 10.1016/S0263-8223(97)00038-X.

39. Ebrahimi, F., Salari, E. (2015). A semi-analytical method for vibrational and buckling analysis of functionally graded nanobeams considering the physical neutral axis position. *Computer Modeling in Engineering & Sciences, 105(2),* 151–181.

40. Liew, K. M., Lei, Z. X., Zhang, L. W. (2015). Mechanical analysis of functionally graded carbon nanotube reinforced composites: a review. *Composite Structures, 120,* 90–97. DOI 10.1016/j.compstruct.2014.09.041.

41. Jiao, P., Chen, Z., Ma, H., Zhang, D., Ge, P. (2019). Buckling analysis of thin rectangular FG-CNTRC plate subjected to arbitrarily distributed partial edge compression loads based on differential quadrature method. *Thin-Walled Structures, 145,* 106417. DOI 10.1016/j.tws.2019.106417.

42. Keleshteri, M. M., Asadi, H., Aghdam, M. M. (2019). Nonlinear bending analysis of FG-CNTRC annular plates with variable thickness on elastic foundation. *Thin-Walled Structures, 135,* 453–462. DOI 10.1016/j.tws.2018.11.020.

43. Duc, N. D., Cong, P. H., Tuan, N. D., Tran, P., Thanh, N. V. (2017). Thermal and mechanical stability of functionally graded carbon nanotubes (FG CNT)-reinforced composite truncated conical shells surrounded by the elastic foundations. *Thin-Walled Structures, 115,* 300–310. DOI 10.1016/j.tws.2017.02.016.

44. Malekzadeh, P., Zarei, A. R. (2014). Free vibration of quadrilateral laminated plates with carbon nanotube reinforced composite layers. *Thin-Walled Structures, 82,* 221–232. DOI 10.1016/j.tws.2014.04.016.

45. Rafiee, M., He, X. Q., Liew, K. M. (2014). Non-linear dynamic stability of piezoelectric functionally graded carbon nanotube-reinforced composite plates with initial geometric imperfection. *International Journal of Non-Linear Mechanics, 59,* 37–51. DOI 10.1016/j.ijnonlinmec.2013.10.011.

46. Alibeigloo, A. (2013). Static analysis of functionally graded carbon nanotube-reinforced composite plate embedded in piezoelectric layers by using theory of elasticity. *Composite Structures, 95,* 612–622. DOI 10.1016/j.compstruct.2012.08.018.

47. Shen, H. S. (2009). Nonlinear bending of functionally graded carbon nanotube-reinforced composite plates in thermal environments. *Composite Structures, 91(1),* 9–19. DOI 10.1016/j.compstruct.2009.04.026.

48. Kwon, H., Bradbury, C. R., Leparoux, M. (2011). Fabrication of functionally graded carbon nanotube-reinforced aluminum matrix composite. *Advanced Engineering Materials, 13(4),* 325–329. DOI 10.1002/adem.201000251.

49. Yang, S., Yu, S., Kyoung, W., Han, D. S., Cho, M. (2012). Multiscale modeling of size-dependent elastic properties of carbon nanotube/polymer nanocomposites with interfacial imperfections. *Polymer, 53(2),* 623–633. DOI 10.1016/j.polymer.2011.11.052.

50. Zhang, H., Cai, P. Z., Zhao, D. L., Shen, Z. M. (2011). Fabrication and mechanical properties of carbon nanotubes reinforced epoxy resin matrix composites. *Journal of Beijing University of Chemical Technology (Natural Science), 38(1),* 62–67.

51. Gao, Y. S., Zhang, S. Q., Huang, Z. T. (2019). Nonlinear modeling and simulation of carbon nanotube fiber reinforced composite plate. *Journal of Mechanical Engineering, 55(8),* 80–87. DOI 10.3901/JME.2019.08.080.

52. Zhang, L. W., Song, Z. G., Liew, K. M. (2015). Nonlinear bending analysis of FG-CNT reinforced composite thick plates resting on Pasternak foundations using the element-free IMLS-Ritz method. *Composite Structures, 128,* 165–175. DOI 10.1016/j.compstruct.2015.03.011.